




# Effect of the laser fluence on the microstructure and the relating magnetic properties of BaFe<sub>12</sub>O<sub>19</sub> films grown on YSZ(111) by PLD for optimized perpendicular recording

Berkin Nergis<sup>1</sup>, Sondes Bauer<sup>1,\*</sup> , Xiaowei Jin<sup>2</sup>, Klaus Seemann<sup>3</sup>, Lukas Horak<sup>4</sup>, Reinhard Schneider<sup>2</sup>, Vaclav Holy<sup>4</sup>, Sven Ulrich<sup>3</sup>, and Tilo Baumbach<sup>1,5</sup>

<sup>1</sup>Institute for Photon Science and Synchrotron Radiation, Karlsruhe Institute of Technology, Hermann-Von-Helmholtz-Platz 1, 76344 Eggenstein-Leopoldshafen, Germany

<sup>2</sup>Laboratory for Electron Microscopy, Karlsruhe Institute of Technology, Engesserstr. 7, 76131 Karlsruhe, Germany

<sup>3</sup>Institute for Applied Materials, Karlsruhe Institute of Technology, Hermann-Von-Helmholtz-Platz 1, 76344 Eggenstein-Leopoldshafen, Germany

<sup>4</sup>Department of Condensed Matter Physics, Charles University, Ke Karlovu 5, 121 16, Prague 2, Czech Republic

<sup>5</sup>Laboratory for Applications of Synchrotron Radiation, Karlsruhe Institute of Technology, Kaiserstr. 12, 76131 Karlsruhe, Germany

Received: 22 August 2022

Accepted: 8 December 2022

Published online:

1 January 2023

© The Author(s) 2022

## ABSTRACT

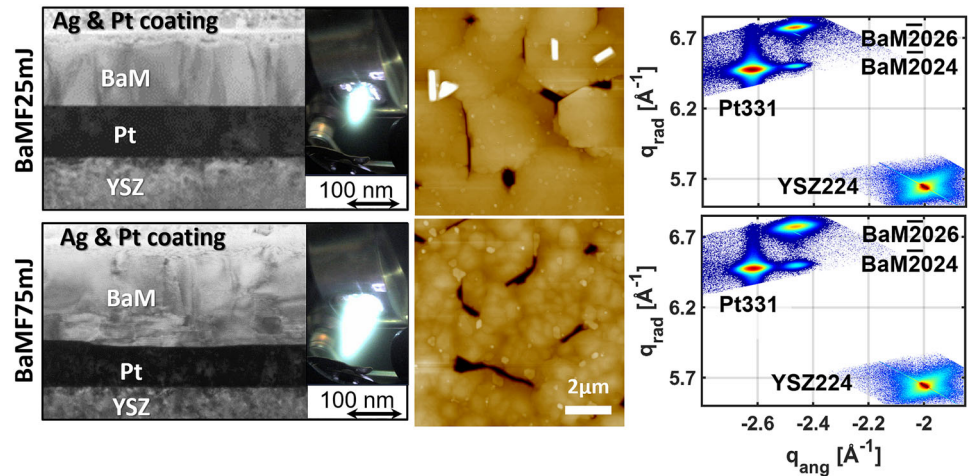
High-quality BaFe<sub>12</sub>O<sub>19</sub> (BaM) films with high uniaxial anisotropy fields of  $H_A = 17.5$  and  $18.5$  kOe were obtained by pulsed laser deposition (PLD) at two fluences of  $1.5$  and  $5.1$  J/cm<sup>2</sup> on YSZ(111) substrate, using a platinum interlayer for reducing lattice mismatch. We demonstrated that the microstructure, morphology, and stoichiometry of the hexaferrite BaFe<sub>12</sub>O<sub>19</sub> films can be affected by raising the corresponding energy per pulse from  $25$  to  $75$  mJ. However, we also concluded that the increase of fluence leads to the formation of a non-stoichiometric BaM film through two nucleation steps and an output growth of small grains in addition to the increase of the defect density. In turn, this has contributed to the enhancement of the coercive field from  $H_c = 1769$  Oe to  $H_c = 2166$  Oe as it is required for the improvement of perpendicular recording resolution. We found that both the lateral coherent block size and misorientation of mosaic blocks are remarkably affected by the growth kinetics, which itself depends on the energy per pulse. For a deep understanding of the effect of laser fluence on the microstructure, chemical composition, and on the magnetic properties of thin BaM films, the results of complementary methods are combined. These methods comprise high-resolution X-ray diffraction, atomic force microscopy, high-resolution transmission electron microscopy (TEM), scanning

Handling Editor: David Cann.

Address correspondence to E-mail: [sondes.bauer@kit.edu](mailto:sondes.bauer@kit.edu)

TEM combined with energy-dispersive X-ray spectroscopy, and vibrating sample magnetometer.

## GRAPHICAL ABSTRACT



## Introduction

Hexagonal barium ferrite with magnetoplumbite structure, i.e.,  $\text{BaFe}_{12}\text{O}_{19}$ , is an important material for applications involving high-density perpendicular as well as longitudinal magnetic recording media [1–4], spintronic devices [5], microwave circuits [6–8], and microwave-assisted magnetic recording (MAMR) [9] because of the recorded large uniaxial magnetic anisotropy  $H_A$ , relatively high permeability and low conduction losses. Workers interested in microwave applications have emphasized epitaxial growth of thick (several  $\mu\text{m}$ ), c-axis oriented, nearly single-crystal films for the construction of microwave filters and other devices. Those interested in magnetic recording have focused on the preparation of c-axis magnetic layers with thickness typically ranging from a few tens of nm to 200 nm as potential perpendicular recording media. For high-density perpendicular magnetic recording (PMR), the media should possess a chemical stability, mechanical durability, moderate hard magnetic properties, and small grains. In order to achieve higher signal-to-noise (S/N) ratio in perpendicular recording media,

highly oriented perpendicular magnetic recording layers with relatively high perpendicular coercivity  $H_C$ , small-grained films, and large perpendicular squareness ( $S_{\perp} = M_{r\perp}/M_{s\perp}$ ) are required [1–3]. Recently,  $\text{BaFe}_{12}\text{O}_{19}$  material can become a promising candidate for multiferroic ceramics [10] and thin film [11] because it is showing strong ferromagnetic and ferroelectric behavior at room temperature. Furthermore, the structure, electrical and magnetic properties of some doped barium hexaferrites have been well investigated, some results suggest excellent magnetoelectric coupling performance in  $\text{BaFe}_{12}\text{O}_{19}$  [12]. Out-of-plane C-axis BaM films have been successfully fabricated by different methods, such as molecular beam epitaxy (MBE) [13, 14], liquid phase epitaxy (LPE) [15], alternating target laser ablation deposition (ATLAD) [16, 17], and radio frequency (RF) magnetron sputtering [18, 19]. There is a remarkable increase of pulsed laser deposition (PLD) growth of high-quality BaM films, which meet the requirement of the aforementioned applications with the focus to investigate the influence of the process parameter on the structure and the magnetic properties [20–26]. C-axis BaM films have been fabricated by PLD on various substrates, like  $\text{Al}_2\text{O}_3(0001)$ ,

MgO(111), SiC(0001), Si(111), GaN(0001), and Gd<sub>3</sub>Ga<sub>5</sub>O<sub>12</sub>(111) [references cited in 8]. It was found that a Pt(111) interlayer was the most effective solution to block the interdiffusion between the substrate and the BaM layer [27–30], and therefore, the performance of excellent *c*-axis orientations. This promotes the magnetic layer growth with the easy magnetization direction perpendicular to the substrate. To the best of our knowledge, BaM was not previously grown on YSZ(111) substrate but rather on Si coated with YSZ and YSZ substrate with (001) orientation [31, 32]. While the influence of the process gas (i.e., oxygen) pressure [21, 25, 26, 33], the substrate surface properties, and substrate temperature [21, 26] on the microstructure, morphology, and magnetic properties of BaM has been previously investigated, the role of laser beam parameters such laser frequency, spot size, wavelength, and fluence has not been extensively studied for ferrite materials [34]. Specifically, the laser fluence controls the deposition rate and the kinetic energy of the ablated species from the target. Ojeda et al. [35] have discussed about the influence of the laser fluence, when the value is close or much higher than the threshold ablation, on the film composition in different systems such as SrTiO<sub>3</sub> or LiCoO<sub>2</sub>, and BaTiO<sub>3</sub>. The O<sub>2</sub> background gas is often used to incorporate oxygen into the film and to moderate the kinetic energy of the arriving species. There is a fundamental interdependence between the laser fluence and the background gas pressure in the PLD process, in order to achieve the optimum kinetic energies of the arriving species to the substrate [35]. Several phenomena take place in the plume such as intra-plume collisions, electrostatic interactions (ions and electrons), and diffusion by the background gas. The species ablated from the target will have different radial distribution depending on their kinetic energy and on their masses. This will in turn affect the local nucleation, growth kinetics, composition, stoichiometry, film thickness, and morphology [36, 37]. In the case of BaM, the increase of the laser fluence will lead to an increase of the number of emitted ion species and the velocity of the species, and therefore, of the kinetic energy distribution of Ba twice as much than Fe because of the atomic mass ratio. The use of higher fluence will give Ba atoms remaining kinetic energy for diffusing on the film surface. Furthermore, the ablation rate in terms of removed material depth (nm) increases with the laser fluence as it was calculated and experimentally

verified by Fähler et al. [38]. Schou [39] has revealed the complicated aspect of the laser ablation and plume expansion and has reported competitive mechanisms, occurring in the stoichiometric transfer from the target to the film. He explained how these competing processes and the resulting film morphology are strongly and dually dependent on the laser fluence as well as the chosen gas background pressure. Zhuang et al. [40] discussed the importance of the stoichiometry on the magnetic properties and microstructure on barium ferrite films grown by RF sputtering. Recently, Yu et al. [34] investigated the evolution of the stoichiometry, phase, and texture of PLD-grown hexagonal barium ferrite films by varying the laser fluence and grew films with the same number of shots. They showed that the grain sizes, crystalline structure, as well as magnetization hysteresis are strongly affected by the chosen fluence without taking the difference of the film thickness into consideration due to the increase of the fluence at a fixed number of shots.

We present a comprehensive study of the effect of laser fluence by changing the energy per pulse from 25 to 75 mJ on the quality of epitaxial growth of BaM hexaferrite films with comparable film thickness after adjusting the number of laser shots. The resulting films were characterized by using a multiplicity of complementary methods, including vibrating sample magnetometer (VSM), high-resolution X-ray diffraction reciprocal space mapping (HR-RSM), atomic force microscopy (AFM), X-ray photoelectron spectroscopy (XPS), and transmission electron microscopy (TEM) techniques, in particular, TEM diffraction contrast and high-resolution TEM (HRTEM) imaging, as well as scanning TEM (STEM) in combination with energy-dispersive X-ray spectroscopy (EDXS).

## Material and methods

### PLD growth of BaM at two different fluences

Two samples named here BaMF25mJ and BaMF75mJ were similarly grown in the PLD chamber by using two pulse energies of 25 and 75 mJ in two steps. As a first step, an interlayer of platinum Pt(111) with a thickness of about 75 nm was grown in vacuum after heating up the substrate to  $T_g = 900$  °C on the yttria-

stabilized zirconia with (111) orientation. A laser pulse energy of 60 mJ and laser repetition rate of 5 Hz was used. As a second step, a hexaferrite target BaFe<sub>12</sub>O<sub>19</sub> from the company surface (99.95% purity) was ablated with a laser repetition rate of 1 Hz by using two different pulse energies for BaMF25mJ and BaMF75mJ in an oxygen background pressure of 400 mTorr at a target-substrate distance of 40 mm. It is worthwhile to emphasize that our investigation on the influence of laser frequency on the growth kinetics, film morphology of LuFeO<sub>3</sub> grown on YSZ(111) [41], and on the crystalline quality favors the use of laser frequency of 1 Hz for the PLD growth. In fact, it demonstrates that the increase of the laser repetition rate from 1 to 10 Hz induces more defect density and degrades the crystalline quality as shown by HRTEM. Even though, the growth at 1 Hz is slow, the crystalline quality was less affected by the defects such as stacking faults and out-of-phase boundaries.

The laser energy was measured with a detector in front of the access view port of the chamber. The energy per pulse was adjusted to 25 and to 75 mJ by regulating the temperatures of the two omega and four omega harmonics of the YaG laser. In order to calculate the fluence, the spot area on the target was determined from the beam imprints at the thermal paper sheets placed at the target position in the chamber. The corresponding fluences were 1.5 and 5.1 J/cm<sup>2</sup>. In order to produce BaMF25mJ and BaMF75mJ films with the same thickness of about 140 nm, the number of 20,000 and 6666 shots was used, respectively. All the PLD growth parameters are summarized in table (S1) (see supplementary information).

### High-resolution reciprocal space mapping (HR-RSM) by symmetric and asymmetric X-ray diffraction

The crystalline structure in terms of in-plane and out-of-plane lattice parameters as well as the mosaicity was determined by means of HR-RSM of a series of BaM symmetric (i.e., (004), (006), (008), (0010), (0012), (0014), (0016), (0022), (0024)) and two asymmetric reflections (i.e., (-2022) and (-2024)). The latter were recorded by a linear Mythen detector of the beamline NANO at the Kara facility in Karlsruhe, Germany. All the HR-RSMs were performed by rocking the sample around the corresponding diffraction angles.

Bauer et al. [42] described the experimental setup in detail which includes the heavy-duty diffractometer, the in situ PLD chamber, and the X-ray beam specifications. We used an X-ray energy of 15 keV and a distance sample detector of 1114 mm, in order to define an angular resolution of 0.0027 degree per channel. In order to ensure a reliable comparison between the microstructure of BaMF25mJ and BaMF75mJ and to perform the corrections for background subtraction, misalignment, and peak intensities, three reflection orders were measured for the substrate, namely YSZ(111), YSZ(222), and YSZ(333) and for the platinum interlayer Pt(111), (222), and (333).

In addition to HR-RSMs of the above-mentioned reflections, we recorded the complete diffraction curves of the films BaMF25mJ and BaMF75mJ by moving the sample and the detector in theta/2theta configuration simultaneously. A comparison between them is shown in Fig. 1, in order to explore the existence of any secondary phase. In Fig. 2, three selected HR-RSMs of (006), (0014), and (0024) from the reflection series are presented for both films, BaMF25mJ and BaMF75mJ, as an example to explain the data analysis procedure applied for both samples. From each individual HR-RSM of BaM reflection order (*00l*), two different cuts, corresponding to the radial and the angular diffraction profiles, were derived and compared in Figs. 3 and 4, respectively. The diffraction profiles for both samples were analyzed by applying the mosaicity model with respect to radial broadening, which comes from the out-of-plane strain fluctuation and from the vertical coherent blocks size, while the angular broadening is the convolution of the broadening due to the lateral block size and to the misorientation of the blocks. All the diffraction profiles were fitted using the origin software package by means of a pseudo-Voigt function, which gives R-square values of 0.99 in comparison with the fitting with the Gaussian and Lorentz functions where R-square values were lower. The peak positions determined from symmetric and asymmetric reflections were utilized to derive the out-of-plane and in-plane lattice parameters and the lattice mismatches between the YSZ(111) substrate and the Pt underlayer and between the BaM layer and the Pt interlayer (see Table 1). The variation of the FWHM<sub>ang</sub> (resp. FWHM<sub>rad</sub>) as function of the reflection order (*00l*) is equivalent to the Williamson-Hall (WH) plot [43] and enables the separate



**Figure 1** Theta/2theta X-ray diffraction scans of BaMF25mJ and BaMF75mJ films showing highly *c*-axis oriented BaM films. The red triangles indicate the peak positions of a minor secondary phase, having Bragg positions closed to the  $\text{Fe}_2\text{O}_3$  phase.

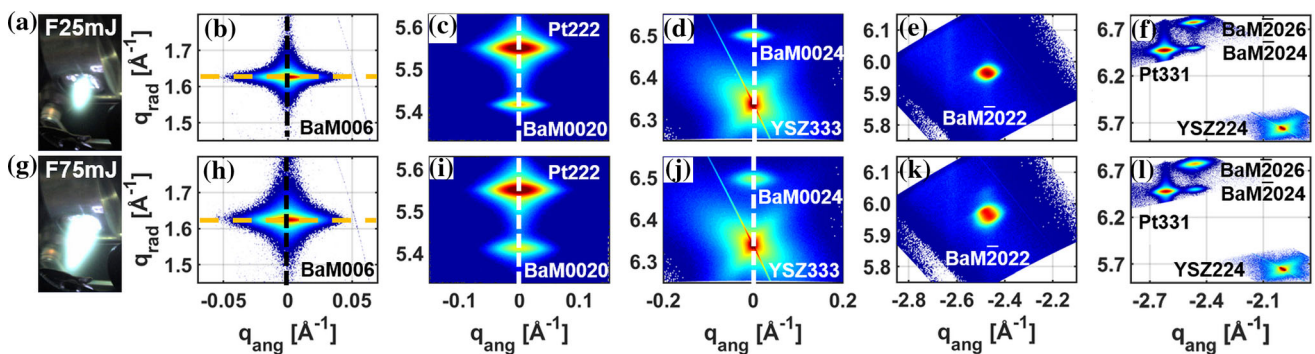
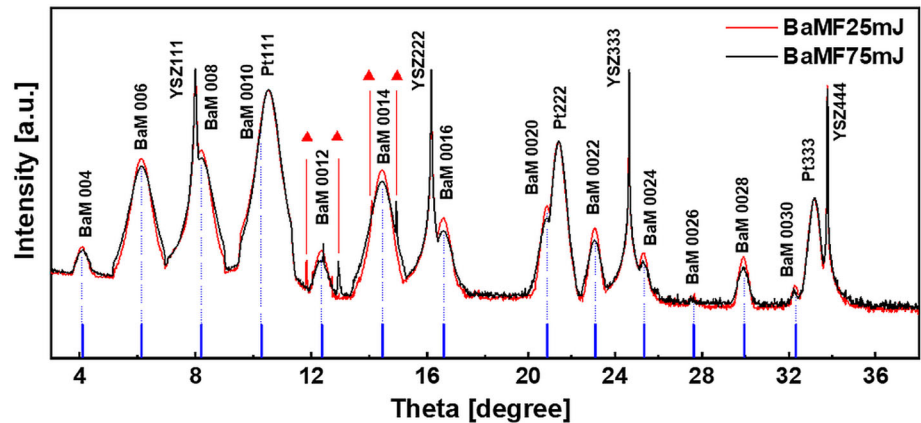


**Figure 2** a & g Plume pictures during the growth of the samples. Selected HR-RSMs of BaM symmetric b & h (006), c & i (0020) together with Pt (222), d & j (0024) together with YSZ(333) and asymmetric e & k (-2022) reflections and f & l (-2024), (-2026) together with Pt(331) and YSZ (224) of BaMF25mJ and

BaMF75mJ films on the upper and lower row, respectively. b Orange and black dashed lines show exemplary cuts for angular and radial diffraction profiles, respectively. c & i and d & j show that *c*-axes of Pt(111) & BaM(0001) films and YSZ(111) & BaM(0001) film are parallel to each other, respectively.

determination of the lateral coherent block size  $L_{\perp}$  (resp. vertical coherent block size  $L_{\parallel}$ ) from the intercept  $Y_0$  at zero coordinate and the misorientation  $\Delta$  (resp. the strain fluctuation  $\varepsilon$ ) from the slope of WH-plots. The derived microstructure parameters are summarized in Table 1.

### Atomic force microscopy in topography mode

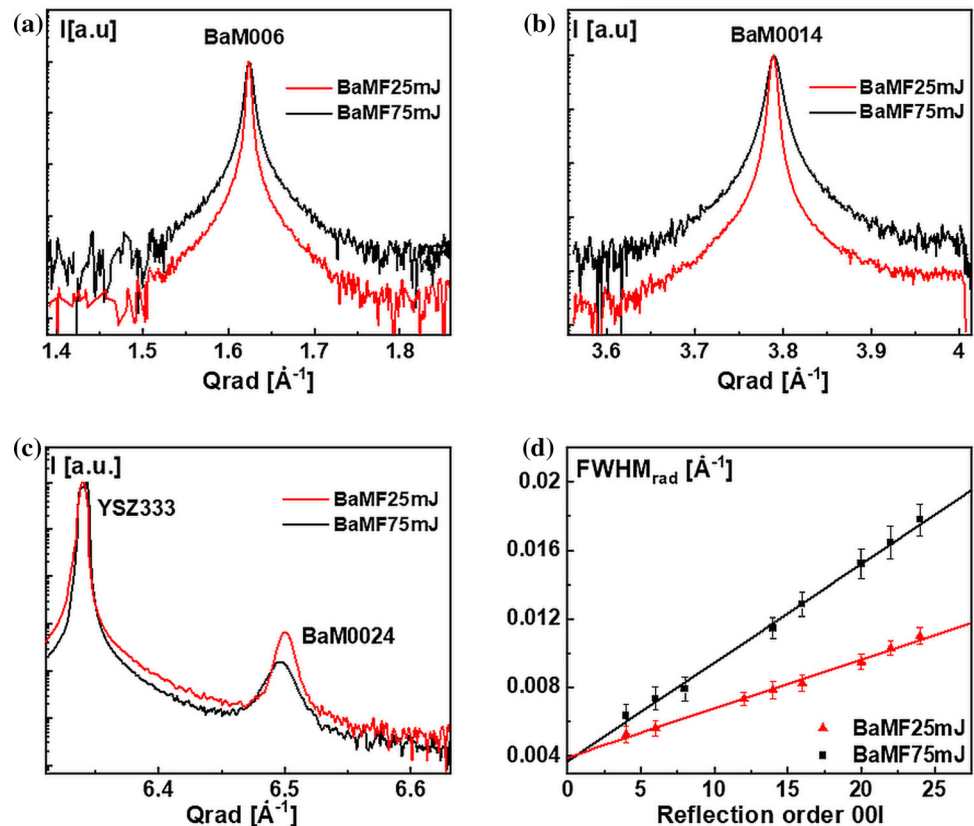
AFM topography measurements were carried out by using a Dimension Icon AFM (Veeco Inc, USA) in tapping mode. As a probe, we used OPUS HQ:NSC15/Al BS cantilevers (NanoAndMore, Wetlar, Germany) with a force constant of 40 N/m and a resonance frequency of 325 kHz. AFM images were analyzed by using the NanoScope software package (Bruker, Karlsruhe, Germany). Particle size analysis on AFM images was carried out by modulating the color scale in black-white to visualize borders of the

particles. 3D topography images were generated by using height sensor data.

### Sample preparation for transmission electron microscopy

Structural properties and the chemical composition of the two films, BaMF25mJ and BaMF75mJ, were studied by conventional TEM, HRTEM, and scanning TEM combined with EDXS. For this purpose, electron transparent cross section specimens were prepared by focused ion beam (FIB) milling using a Helios NanoLab G4 FX dual-beam instrument (Thermo Fisher Scientific). Before FIB preparation of the TEM lamellas, a thin metal layer of gold or silver was sputtered on the sample surface by means of a Leica sputter coater to protect the BaM films from ion beam damage. Then, as usual for FIB preparation, an additional Pt/C protection layer was deposited on top of this metal layer. Coarse FIB milling was carried

**Figure 3** Radial diffraction profiles of selected BaM RSMs of **a** (006), **b** (0014), and **c** (0024) reflections together with YSZ(333) reflection of BaMF25mJ and BaMF75mJ. **d** Williamson-Hall plot of  $\text{FWHM}_{\text{rad}}$  as function of the reflection order (00l).



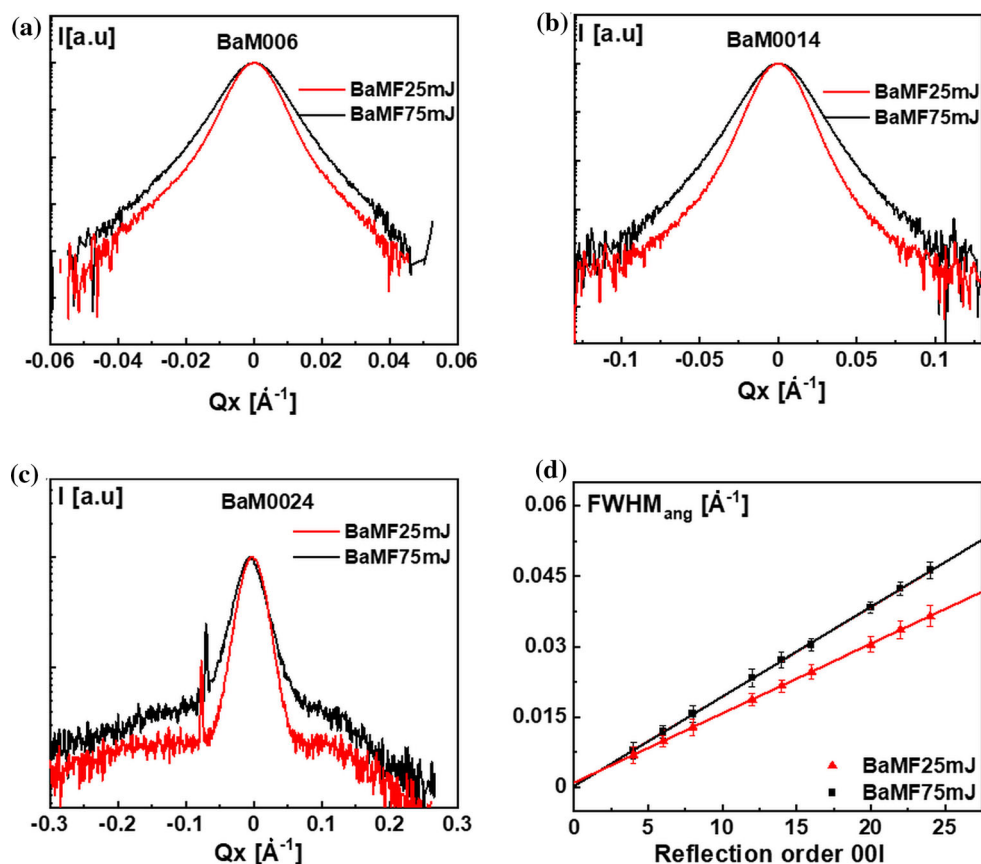
out with  $\text{Ga}^+$  ions at an accelerating voltage of 30 kV, whereas for final polishing of the sample surfaces (ca. 5000 scans at each side), 5 kV with approximately 70 pA ion current was used.

### Analytical transmission electron microscopy (TEM)

TEM investigations of the BaM films were carried out on two different transmission electron microscopes possessing a thermally assisted field emission cathode (Schottky emitter). In more detail, an aberration-corrected FEI Titan3 80–300 microscope was used for conventional TEM and HRTEM imaging for the general layer properties (e.g., layer thickness, crystal structure) as well as for determining specific microstructural phenomena (Pt/BaM interface, crystal defects). Due to the spherical aberration corrector in the imaging system of the Titan microscope, in HRTEM, a point resolution of 0.08 nm can be achieved. For image recording, the microscope is equipped with a  $4 \text{ k} \times 4 \text{ k}$  CMOS camera of the F436 type (TVIPS). Selected area electron diffraction (SAED) was used to determine the crystal orientation of BaM and Pt interlayer. Microchemical EDXS

analyses were carried out by using a 200 kV microscope of the type FEI Tecnai Osiris. This microscope is equipped with a Super-X EDXS detector (FEI) which combines four silicon drift detectors (SDD). X-ray maps were recorded in the STEM mode via the so-called HyperMap mode of the ESPRIT software (Bruker). Typical measurement times were in the range from 60 to 90 min., where a possible drift of the sample was automatically corrected by cross-correlation of corresponding reference images. STEM images were taken by means of a high-angle annular dark-field (HAADF) detector for which the image brightness is a function of the mean atomic number. For combined STEM/EDXS analyses, the lateral resolution amounted to approximately 1 nm in accordance with spot size no. 6 and the use of a condenser aperture of 100  $\mu\text{m}$  in diameter. By employing the ESPRIT 2.3 software, the raw-data X-ray maps were quantified by using the thin-film approximation after Cliff-Lorimer [44] to obtain element-concentration maps and the corresponding line profiles.

**Figure 4** Angular diffraction profiles of selected BaM RSMs of **a** (006), **b** (0014) and **c** (0024) reflections of BaMF25mJ and BaMF75mJ. **d** Williamson-Hall plot of  $\text{FWHM}_{\text{ang}}$  as function of the reflection order ( $00l$ ).



### X-ray photoelectron spectroscopy (XPS)

XPS measurements were performed at the IPS UHV analysis laboratory by using a Phoibos 150 analyzer and an unmonochromated XR-50 Mg  $K_{\alpha}$  X-ray source from SPECS. The angle between the analyzer and the X-ray source was fixed to  $45^\circ$ . The pressure inside the analysis chamber was about  $3 \times 10^{-10}$  mbar. All measurements were carried out at room temperature with the pass energy of 20 eV and an energy step of 0.05 eV. The deconvolution of the peaks was performed by the Fityk software using Voigt profiles and by applying a linear background. This linear background is more suited to our BaM films as insulating materials rather than the Shirley background which is more adapted to the case of metallic layers, as it has been reported in the CasaXPS manual [45, 46]. The binding energy was calibrated by using the Au  $4f_{7/2}$  (84.00 eV) photoemission line of a corresponding reference material [47]. Due to the charging effect, the

adventitious C 1s (284.5 eV) was acquired as an additional calibration of the binding energy [48]. The fitting process for all components corresponding to the different chemical elements like Ba, Fe, and O was carried out by constraining the full width half maximum FWHM to a constant value. The fitting parameters of all components are given in table (S2) of the supplementary information.

### Vibrating sample magnetometry (VSM)

The magnetic in-plane and out-of-plane magnetization loops were measured by using a VersaLab vibrating sample magnetometer from Quantum design with a magnetic field up to 3 Tesla. The measurements were performed for both samples, BaMF25 and BaMF75mJ, at room temperature only. From the magnetization loops, the saturation magnetization  $M_s$ , the remanent magnetization  $M_r$ , the perpendicular and parallel squareness's  $S_{\perp} = M_{r\perp}/$

**Table 1** In and out-of-plane lattice parameters of YSZ(111), Pt(111) and BaFe<sub>12</sub>O<sub>19</sub> film together with the in-plane mismatch between YSZ(111) / Pt(111) and Pt(111) / BaM

	YSZ(111)		Pt(111)		BaFe <sub>12</sub> O <sub>19</sub>		Mismatch	
	In-plane lattice parameter a (Å)	Out-of-plane lattice parameter c (Å)	In-plane lattice parameter a (Å)	Out-of-plane lattice parameter c (Å)	In-plane lattice parameter a (Å)	Out-of-plane lattice parameter c (Å)	(YSZ/Pt) (%)	(Pt/BaM) (%)
BaMF25mJ	7.2807 ± 0.0001	5.1481 ± 0.0001	5.5449 ± 0.0001	3.9255 ± 0.0001	5.8632 ± 0.0001	23.2001 ± 0.0001	23.841 ± 0.001	5.740 ± 0.002
BaMF75mJ	7.2833 ± 0.0001	5.1400 ± 0.0001	5.5452 ± 0.0001	3.9218 ± 0.0001	5.8396 ± 0.0001	23.2171 ± 0.0001	23.864 ± 0.001	5.309 ± 0.002

$M_{s\perp}$  and  $S_{//} = M_{r//}/M_{s//}$ , the out-of-plane and in-plane coercivity fields  $H_{c\perp}$  and  $H_{c//}$ , and the coercivities ratio  $H_{c//}/H_{c\perp}$  were derived. All values were determined for the samples BaMF25mJ and BaMF75mJ and compared in Table 3.

## Results and discussion

### Effect of the fluence on mosaicity, structure, and strain

The XRD patterns, which correspond to the BaMF25mJ and BaMF75mJ films, are compared in Fig. 1. Both diffraction curves contain the BaM (00l) peaks, fourth order of the YSZ with (111) orientation and three orders of reflection Pt111, Pt222, and Pt333 which belong to the Pt interlayer with (111) orientation. For both samples, BaMF25mJ and BaMF75mJ, the good quality of the BaM films can be deduced from the absence of other peaks than (00l). The comparison of the two XRD profiles shows similar intensities for the Pt(111) underlayer and for the substrate peaks. There is a slight difference in the (00l) diffraction peaks. The diffraction profiles (black line) are broader in the case of BaMF75mJ and the intensities are lower with respect to the diffraction profiles of BaMF25mJ. Furthermore, the XRD curve of BaMF75mJ contains an additional peak with low intensity, lying between BaM0012 and BaM0014 reflections, which is indicated in Fig. 1 by a red triangle symbol. The determined diffraction Bragg angle is not far from that of the Fe<sub>2</sub>O<sub>3</sub> phase. This allows us to conclude that the increase of the fluence from 25 to 75 mJ leads to the formation of a minor Fe<sub>2</sub>O<sub>3</sub> phase and therefore to a stoichiometry fluctuation in the case of BaMF75mJ. Figure 2 illustrates HR-RSMs of selected symmetric and asymmetric reflections. The upper and the lower panels correspond to BaMF25mJ and BaMF75mJ, respectively. The HR-RSM of Fig. 2c, which simultaneously shows the RSMs of Pt222 and BaM0020, demonstrates that the Pt interlayer is well oriented along the c-axis as the BaM layer does not exhibit any detectable misorientation between the Pt(111) and BaM crystallographic planes. In a similar way, HR-RSMs of Fig. 2d which combines the RSMs of YSZ333 and BaM0024 show that the BaM layer is well oriented along the c-axis without any misorientation. In order to evaluate the effect of increasing the



**Table 2** Vertical and lateral blocks sizes obtained by WH-Plots and TEM images, together with misorientation angle and root mean square deviation of strain along the growth direction for BaMF25mJ and BaMF75mJ films

	Vertical coherent block size ( $L_{\perp}$ )	Lateral coherent block size ( $L_{\perp}$ )	Vertical size of mosaic blocks	Lateral size of mosaic blocks	Misorientation angle ( $\Delta$ )	Root mean square deviation of strain ( $\epsilon$ )
Determination method	WH-Plot of SXR (nm)	WH-Plot of SXR (nm)	TEM (nm)	TEM (nm)	WH_Plot of SXR (degree)	WH_Plot of SXR
BaMF25mJ	85 ± 3	293.5 ± 29	135	[25–156]	0.626 ± 0.1	2.86E-4 ± 0.10E-4
BaMF75mJ	85 ± 5	925 ± 92	[6 – 122]	[23–244]	0.804 ± 0.1	5.75E-4 ± 0.16E-4

fluence from 25 to 75 mJ, HR-RSMs were analyzed by following the procedure described in the experimental section above. Figure 3 merely shows the comparison between the radial diffraction profiles of selected reflections BaM006, BaM0014, BaM0024 illustrated in Fig. 3a, b, and c, respectively. The latter show higher radial broadening in the case of BaMF75mJ. In order to interpret the effect of the fluence on the radial broadening, we described the BaM microstructure by means of the mosaic blocks where the radial broadening results from the convolution of the out-of-plane strain fluctuation and vertical size of the blocks. By applying the WH-plot in Fig. 3d, we found out that the root mean square deviation of the strain  $\epsilon = 5.75 \cdot 10^{-4}$  derived from the slope of WH-plot is higher in the case of BaMF75mJ (see Table 1). It should be emphasized that the slope of WH-plot depends on the strain fluctuation inside the grown film. The vertical sizes of the mosaic blocks for BaMF25mJ and BaMF75mJ have comparable values of about 85 nm. In the WH-plot approach, the size distribution of the mosaic blocks is monodispersed. Furthermore, the radial broadening could be also interrelated with the quality of the crystal structure. By comparison with BaMF25mJ, Fig. 3 clearly demonstrates a larger radial broadening in the case of BaMF75mJ, which could be related to a stoichiometry fluctuation. Figure 3c reveals a shift in the peak position of the BaM0024 reflection to lower wave vector values by increasing the fluence from 25 to 75 mJ. In fact, the out-of-plane lattice parameter has increased from  $c = 23.2001$  to  $c = 23.2171$  Å, and the in-plane lattice parameter has decreased from  $a = 5.8632$  to  $a = 5.8396$  Å, most probably due to the variation in the composition (oxygen and cations) in the BaMF25mJ and BaMF75mJ layers. This led to the decrease of the mismatch value from 5.740% to 5.309% between the Pt interlayer and the BaM layer

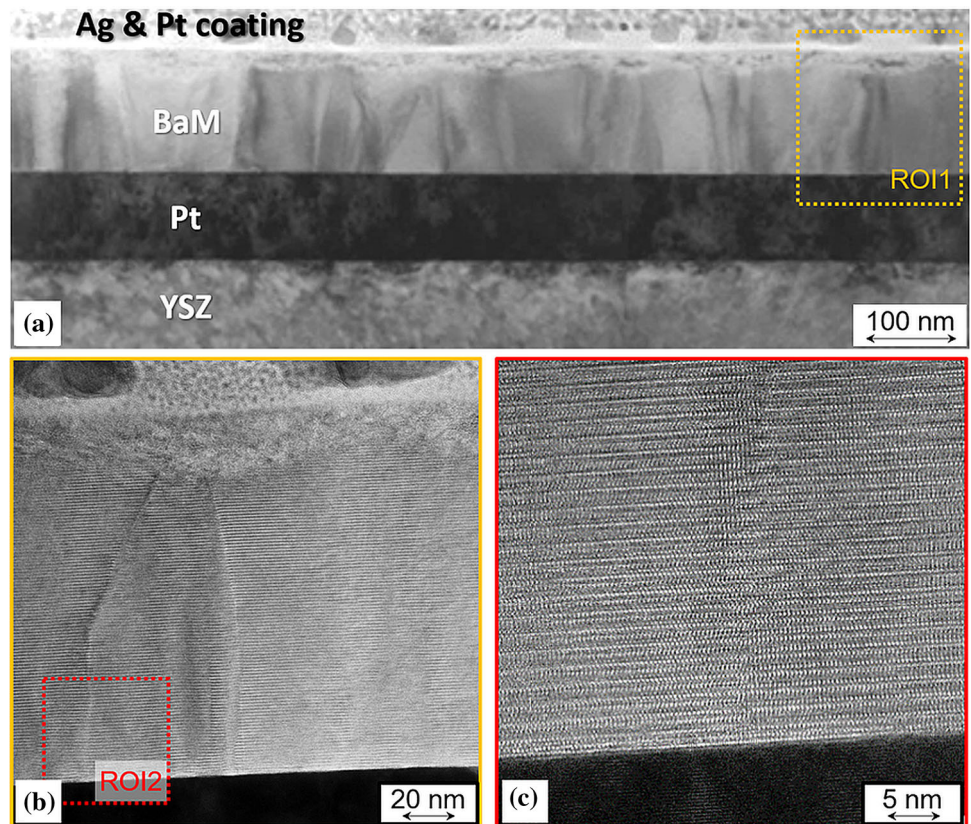
(see Table 1). Additionally, the formation of a minor  $\text{Fe}_2\text{O}_3$  phase in the case of BaMF75mJ could lead to the increase of the strain fluctuation from  $\epsilon = 2.86\text{E-}4 \pm 0.10\text{E-}4$  for BaMF25mJ to  $5.75\text{E-}4 \pm 0.16\text{E-}4$  for BaMF75mJ (see Table 2). Jaber et al. [36] revealed a similar behavior of the  $c$ -parameter in their investigation of the effect of the laser fluence on the structure and composition of  $\text{BiFeO}_3$  grown by PLD on  $\text{SrTiO}_3$ .

Figure 4a, b, and c compares the angular diffraction profiles of the different reflections (006), (0014), and (0024) for the BaMF25mJ and BaMF75mJ samples. The angular broadening is interrelated to the lateral coherent block size and with the misorientation of the mosaic blocks, which is the result of the defect formation in the film (see Table 1). Applying the WH approach in Fig. 4d and assuming a monomodal distribution of the blocks, the lateral block size and the misorientation were found to be larger in the case of BaMF75mJ.

The large angular broadening in the case of BaMF75mJ could originate from a higher density of crystal defects due to the increase of the laser fluence.

Cross sections of both BaM films prepared by FIB milling were also studied by different TEM techniques, in order to elucidate their thickness, homogeneity, structural perfection, and chemical composition. In more detail, diffraction contrast TEM imaging combined with electron diffraction was applied to reveal structural properties of the BaM/Pt layers such as their thicknesses and crystallinity. The structural setup of the interfacial region between BaM and the Pt interlayer as well as of the differently grown BaM films was investigated by means of HRTEM. The chemical composition of the BaM films was analyzed by combined STEM/EDXS experiments. Figures 5 and 6 demonstrate typical results achieved from the BaMF25mJ and BaMF75mJ films,

**Figure 5** **a** Cross-sectional TEM bright-field image of the BaM/Pt layer stack on YSZ(111) substrate of the sample BaMF25mJ, dark vertical lines as well as black/white regions hint at the presence of mosaic blocks that fill the full layer thickness. **b** Corresponding selected area electron diffraction (SAED) pattern representing the orientation relationship between BaM and Pt. **c** High-resolution TEM image of the BaM region ROI1 with three mosaic blocks. **d** Detailed HRTEM image of the interfacial region ROI2 between BaM along its [10] zone-axis direction and Pt along [11-2] in the vicinity to the mosaic-block boundary marked with a square in (g).



which are discussed in detail in the following section. In general, the TEM findings confirm the epitaxial growth of both BaM films, namely BaMF25mJ and BaMF75mJ, on the subjacent Pt interlayers.

In the case of sample BaMF25mJ, the TEM bright-field image in Fig. 5a shows a uniformly grown BaM film with an average thickness of 135 nm on top of a continuous Pt layer. The thickness of the Pt layer amounts to approximately 100 nm. Additionally, the lateral sizes of mosaic blocks were also determined from the TEM bright-field image of Fig. 5a and they were found to be in the range of 25 nm to 156 nm (see column (5) in Table 2).

In Fig. 5b, a SAED pattern is depicted which was taken from the interfacial region between BaM and Pt. Therefore, a superposition of diffraction spots corresponding to both materials can be seen and are marked accordingly. Obviously, there is a good epitaxial growth of BaM on Pt with the (0002) lattice planes of BaM aligned parallel to the (111) Pt planes. This is in accordance with the above-described XRD curves shown in Fig. (1). The BaM film itself exhibits black/white contrast features that mainly appear in form of predominantly vertical lines or

brighter/darker areas, respectively. These features are most likely caused by locally different diffraction conditions and can be attributed to slightly differently orientated crystal regions, i.e., the mosaic blocks, as already found in XRD measurements. Obviously, in the growth direction, the BaM mosaic blocks extend across the full thickness of the film. However, their lateral extension within the film seems to vary locally as deducible from higher magnified TEM micrographs. Exemplarily, Fig. 5c depicts a BaM transition region between three blocks, which is marked by an orange frame in Fig. 5a. The crystal structure of each individual mosaic block appears to be relatively perfect, but the boundaries between them are structurally disturbed due to some slight twist/rotation of one block with respect to the other. The BaM/Pt interfacial region of the left-hand boundary is visualized by HRTEM imaging at a magnification of 1.1 million times (see Fig. 5d). A detailed evaluation yields that the orientation relationship between BaM and Pt seems to be the following: in Fig. 5d, Pt is transmitted along its [11-2] zone axis (ZA) and BaM is in [10] ZA orientation. Thus, the (0002) planes of the BaM film are parallel to

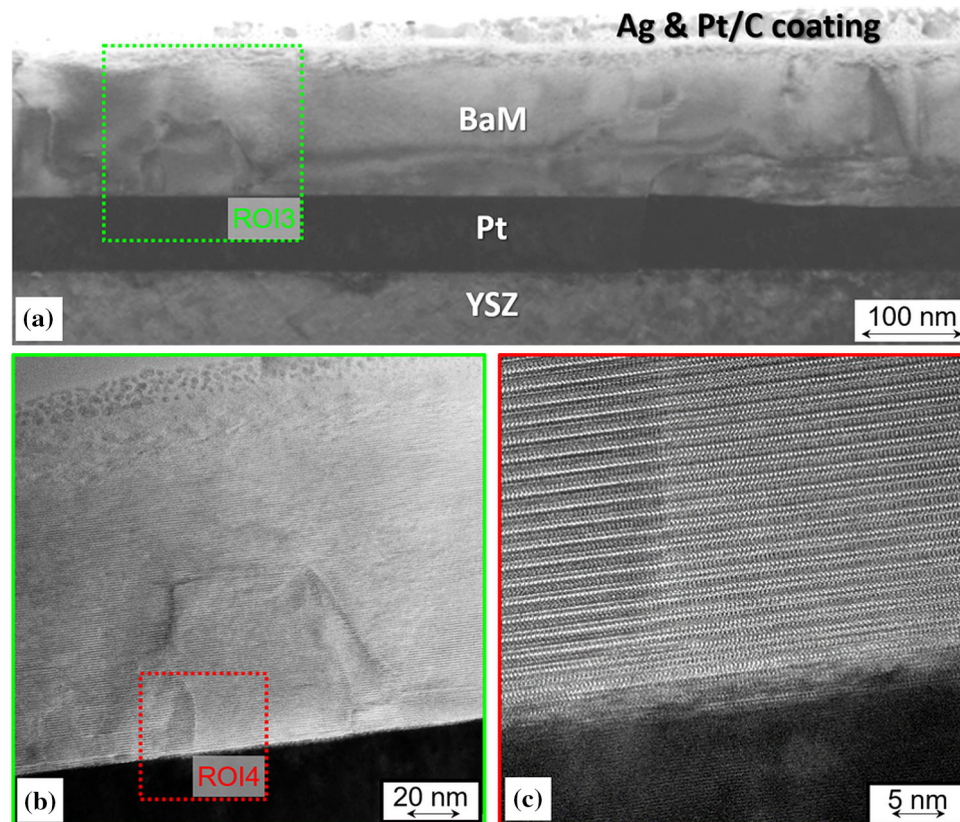


**Figure 6** **a** Cross-sectional TEM bright-field image of the BaM/Pt layer stack on YSZ(111) substrate of the sample BaMF75mJ and **b** corresponding SAED pattern showing the orientation relationship between BaM and Pt. In this BaM film, the bottom region with a vertical extension of about 50 nm appears to be more disturbed than that of sample BaMF25mJ, even horizontally

(111) planes of Pt. Moreover, the hexagonal crystal structure of both BaM mosaic blocks seems to be well developed, but the stacking of lattice planes is evidently different in each block indicating the presence of out-of-phase boundaries. This means that these mosaic-block boundaries are two-dimensional crystal defects. Probably, the individual BaM blocks with corresponding vertical boundaries originate from the lattice misfit between BaM and Pt. In general, the PLD-grown BaM films seem to be single crystalline, but its real structure, i.e., the number of mosaic blocks, and with this, the number of boundaries obviously depend on the laser fluence since the energy per pulse is different during layer growth.

As to BaMF75mJ, Fig. 6 comprises typical TEM results that generally look very similar to those of BaMF25mJ. However, having a closer look reveals some differences, in particular with respect to the number of mosaic blocks and specific types of

separated crystalline blocks are observable. **c** High-resolution TEM image of a complex mosaic-block structure (ROI3) with both vertical and horizontal boundaries within the BaM film. **c** Detailed HRTEM image of the interfacial region (cf. ROI4 in figure (g)) between BaM along its [10] zone-axis direction and Pt along [11-2] exhibiting several mosaic-block boundaries.

boundaries in between. In more detail, the boundaries appear to be more complex, which means that they are partially curved and, in addition, there seem to be horizontal mosaic-block boundaries beside vertical ones. Furthermore, the lateral density of mosaic-block boundaries in BaMF75mJ is probably higher than for BaMF25mJ. In conclusion, this higher defect density in BaMF75mJ is the reason for the large broadening recorded in the angular diffraction profiles (see Fig. 4).

These phenomena can already be seen in the TEM overview image of Fig. 6a, showing an approximately 130 nm thick BaM layer on an 80 nm thick Pt interlayer. Furthermore, the vertical and horizontal sizes of the mosaic blocks were locally measured from the TEM bright-field image of Fig. 6a and were found to be in the ranges [6–122 nm] and [23–244 nm], respectively, as it is illustrated by columns (4) and (5) in Table 2. In Table 2, the block sizes, which were locally measured from TEM overview images of Figs. 5a and 6a for



BaM25mJ and BaM75mJ were found to be larger than the ones, derived from WH approach. This discrepancy could be explained by the fact that XRD data was measured over larger integrated volume while the blocks size derived from TEM images are determined at different specific locations in the film with nm-resolution. Additionally, in the WH approach, the angular broadening of diffraction profiles was assumed to be only related to the lateral coherent blocks size and to the misorientation of the blocks and neglecting the broadening caused by the defects at boundaries.

In Fig. 6b, an SAED pattern of an interfacial region between BaM and Pt is given, which shows a clear epitaxial orientation relationship of  $(0002)\text{BaM} \parallel (111)\text{Pt}$  similar to BaMF25mJ. As an example, Fig. 6c shows details of such horizontal boundaries between single mosaic blocks at a magnification of 165 thousand times. Perhaps, because of the higher energy per pulse of 75 mJ, the time was too short to form a perfect crystal structure during growth of a comparable BaM film with about 130 nm thickness. As can be seen in the HRTEM image of Fig. 6c, likewise to BaMF25mJ, the  $(0002)$  lattice planes of BaM are parallel to  $(111)$  planes of Pt as well. Moreover, the structural setup of vertical mosaic-block boundaries is generally similar to that of sample BaMF25mJ, i.e., the stacking of atomic planes is different in the adjacent BaM blocks. However, there is additional phenomena observable, namely in form of more or less well-defined horizontal blocks with corresponding boundaries in between. In the case of BaMF75mJ, such horizontally separated crystalline blocks seem to be predominantly present in the bottom regions of the BaM film with a vertical extension of about 30 to 50 nm. These regions correlate with zones of cloudy-like image contrast visible in the TEM overview image depicted in Fig. 6a. For the two different BaM films under investigation, apart from the above-described different structural properties, there were also minor differences in the chemical composition found, influenced by the laser fluence used during deposition.

### Effect of the fluence on surface morphology, chemical state, stoichiometry, and on magnetic properties

#### *Surface morphology in dependence on the laser fluence*

Figure 7 compares the surface morphology of BaM grown at 25 and 75 mJ for two different thicknesses

of 70 and 140 nm, in order to understand the evolution as a function of the film thickness and of the laser fluence. The micrographs of the first and of the second columns correspond to 25 and 75 mJ for the film thickness of 70 nm, while micrographs of the third and fourth columns correspond to the film thickness of 140 nm. The micrographs of Fig. (7a, e,f) show well-defined hexagonal grains in the case of 25 mJ. By increasing the fluence, the amount of the energetic species, ablated from the target and then passing through the gas to the substrate and arriving on the substrate surface, becomes higher. This contributed to the interconnection and the coalescence of the hexagonal grains where the boundaries cannot be identified. In conclusion, the resulting BaM morphology is composed of more rounded and elongated grains formed by connected and non-defined hexagonal grains (see Fig. (7b, f, j)). The increase of the film thickness from 70 to 140 nm in the case of 25 mJ leads to an increase of the size of hexagonal grains from 450 to 800 nm (Figures (a, e, i) and (c, g, k)). However, the increase of the thickness in the case of the film grown at 75 mJ leads to the formation of distributed and well-diffused grains in the size range of 80 to 265 nm on the top of formed and interconnected hexagonal chains (see Fig. (7b, f, j) and (7d, h, i)). In conclusion, BaMF75mJ sample displays two types of outgrowths. The first type is composed of large hexagonal interconnected forming chains and the second type consists of spherical grains with a size distribution, which varies between 80 and 265 nm. However, Fig. (7) also shows the presence of smaller grains with a size of about 40 nm for BaMF25mJ. All evidence implies that the film has undergone a two-dimensional growth mode, under which, at the initial stage, a layer-by-layer growth mode is dominating. By increasing film thickness beyond 70 nm, nucleus with high kinetic energy diffuses onto the substrate surface and coalescences to form grains where the sizes are dependent on the flux density and on the laser fluence. Similar BaM morphology was demonstrated by Zhang et al. [40] in the case of BaM grown by PLD with an oxygen pressure of 0.5 mbar (375 mTorr) and a fluence of  $3 \text{ J/cm}^2$  on sapphire  $\text{Al}_2\text{O}_3(0001)$  at a temperature of 780 °C. We can conclude that BaM morphology is strongly influenced by the increase of the fluence from 25 to 75 mJ due to the increase of the diffusion energy on the substrate surface. In order to meet better the requirement of high-density perpendicular recording media, further



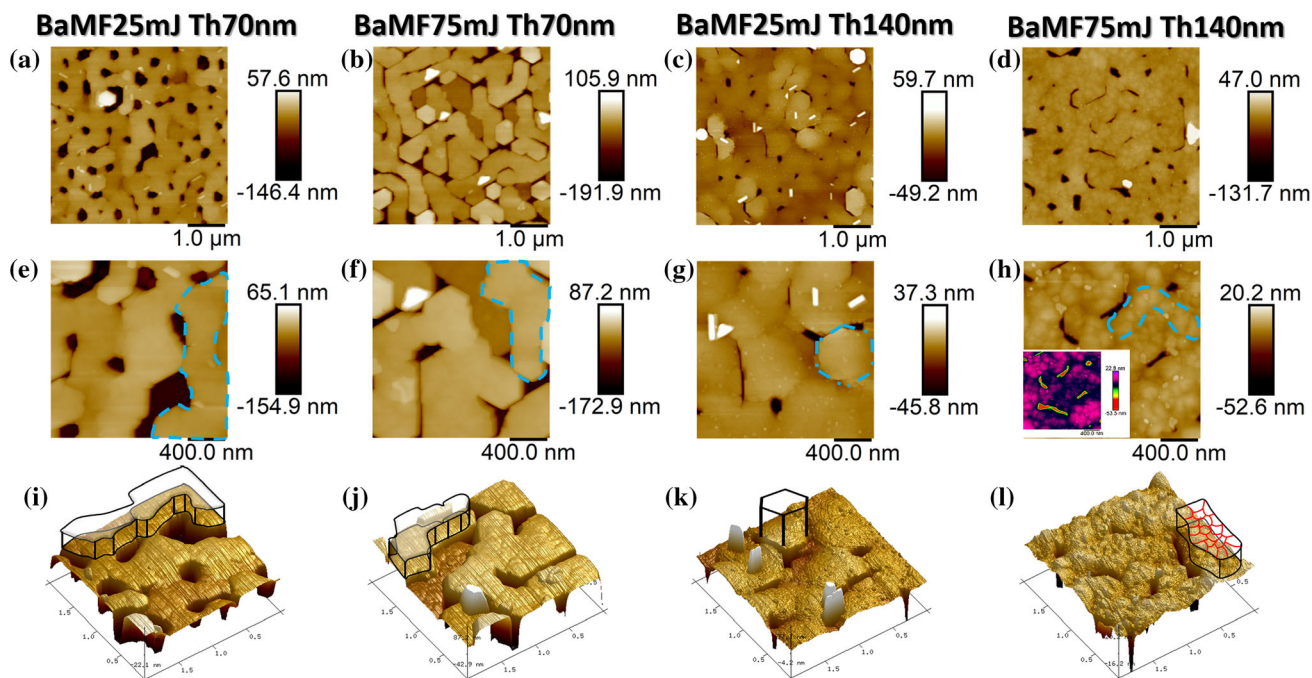


**Figure 7** Atomic force microscopy (AFM) morphology images **a**, **b**, **c**, **d** from 5  $\mu\text{m} \times 5 \mu\text{m}$  region, **e**, **f**, **g**, **h** from 2  $\mu\text{m} \times 2 \mu\text{m}$  region of BaMF25mJ Th70nm, BaMF75mJ Th70nm, BaMF25mJ Th140nm, and BaMF75mJ Th140nm, respectively. Blue dashed lines show typical topography features. **i**, **j**, **k**, **l** show the 3D

images of the corresponding 2  $\mu\text{m} \times 2 \mu\text{m}$  morphology images in **e**, **f**, **g**, **h**, respectively. Representative topographic features are highlighted via extended drawings on 3D topography images (**i**, **j**, **k**, **l**).

tuning of the obtained grain sizes (between 80 and 265 nm) would be necessary in the case of 75 mJ. This could be achieved by growing BaM at oxygen pressure higher than 400 mTorr at the corresponding target-substrate distance, which needs to be determined and examined.

### Surface chemical state and composition in dependence on the laser fluence

Figures 8b, c, and d illustrate the spectra for the Ba 3d, Fe 2p, and O 1s lines recorded on the surface of BaMF25mJ film.

In Fig. 8b, two peaks can fit each of the Ba  $3d_{3/2}$  and Ba  $3d_{5/2}$  of the BaMF25mJ sample. The lower binding energy (BE) of the spin-orbit-split (SOS) pair at  $3d_{3/2}$   $BE_{Ba1} = 793.98 \text{ eV}$  and  $3d_{5/2}$   $BE_{Ba1} = 778.65 \text{ eV}$ , denoted as Ba1 (peak 1 and 3, blue curves), is assigned to Ba1 atoms in the perovskite phase. The higher binding energy SOS pair at  $3d_{3/2}$   $BE_{Ba2} = 795.33 \text{ eV}$  and  $3d_{5/2}$   $BE_{Ba2} = 780 \text{ eV}$ , denoted as Ba2 (peak 2 and 4, red curves), is assigned to Ba2 atoms in a different chemical environment. The energy separation between Ba1 and Ba2 is about

$1.5 \pm 0.1 \text{ eV}$ . Similar XPS spectra of Ba atoms were also recorded by Atuchin et al. [49] in the case of hexaferrite BaM powder samples. The BE, which corresponds to the peak positions of Ba  $3d_{3/2}$  and Ba  $3d_{5/2}$  for the samples BaMF25mJ and BaMF75mJ, is summarized in Table 1 of the supplementary information. Figure 8a and b compares between the Ba spectra of the 25 mJ and 75 mJ, respectively. Both spectra demonstrate the existence of two types of atoms, namely Ba1 and Ba2. However, since the ratio Ba1/Ba2 differs from 1.08 in case of BaMF25mJ to 1.34 in case of BaMF75mJ, this has consequently induced different Ba overall profiles. There is a general agreement that a binding energy of Ba lower than 780 eV corresponds to Ba1 atoms, which belong to the perovskite BaM phase.

As illustrated by Fig. 8c, the XPS spectra of Fe 2p contain the  $2p_{3/2}$  and  $2p_{1/2}$  multiplet given by (peak1, peak2) and (peak3, peak4), respectively, as well as the corresponding satellites. The overall curve fits very well with the measured one. The BE which corresponds to the peak positions of the  $2p_{1/2}$  and  $2p_{3/2}$  multiplet for BaMF25mJ and BaMF75mJ is compared in table (S2-b) of the supplementary

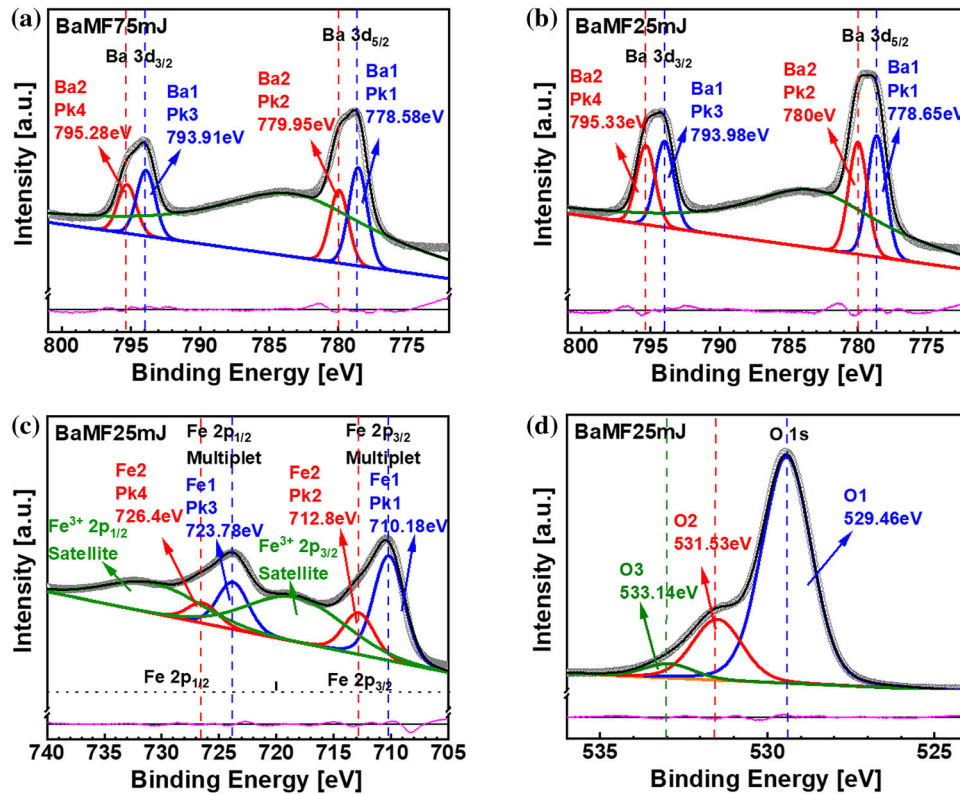


**Figure 8** Measured and fitted narrow range XPS spectra of BaM films, **a** Ba 3d spectra of BaMF75mJ, **b** Ba 3d spectra of BaMF25mJ, **c** Fe 2p spectra of BaMF25mJ, and **d** O 1s of BaMF25mJ. Open circles correspond to measured XPS data where solid black lines correspond to fitted data, orange line represents the background intensity, blue, red, and green curves show the fitting peaks, below the fits solid magenta line corresponds to fit residue. Blue curves of (a,b) correspond to peak 1 (Pk1) and peak 3 (Pk3) of Ba1 doublet where red curves of (a,b) correspond to peak 2 (Pk2) and peak 4 (Pk4) of Ba2 doublet with spin-orbit

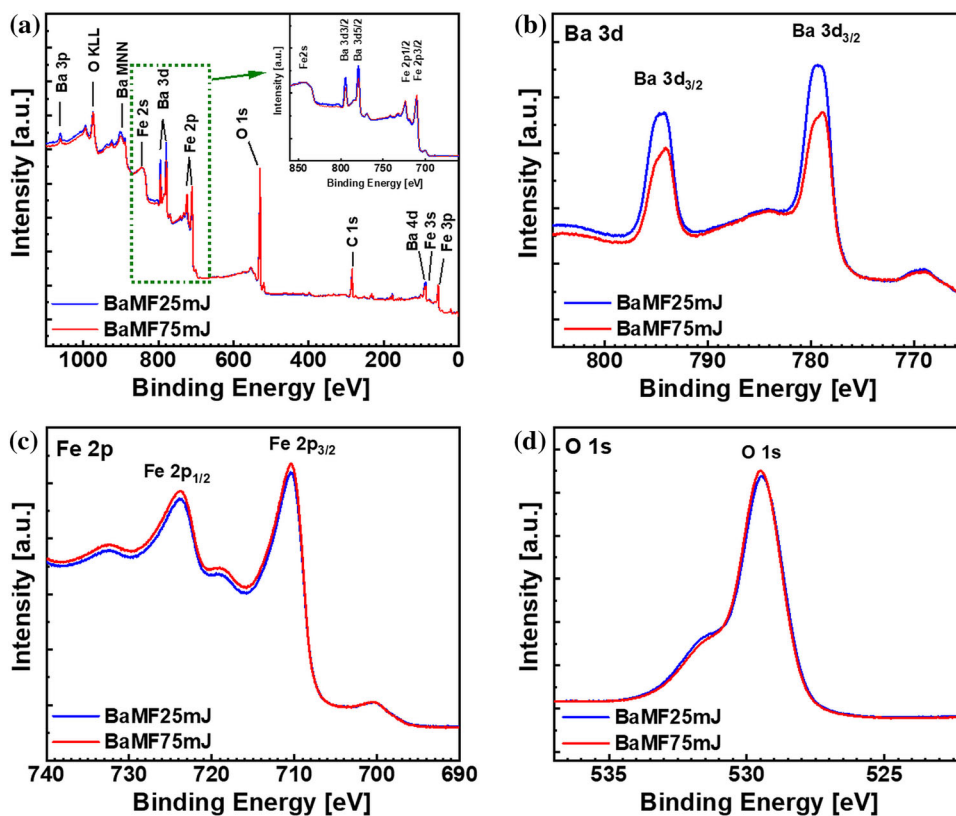
splitting  $SOS = 15.33$  eV, with intensity ratio of  $I_{5/2}:I_{3/2} = 2/3$ . The solid green line in (a,b) corresponds to the Auger peak of Fe LMM. Blue curves in (c) correspond to peak 1 (Pk1) and peak 3 (Pk3) of Fe1 doublet and red curves represent peak 2 (Pk2) and peak 4 (Pk4) of Fe2 doublet separated by  $SOS = 13.6$  eV with intensity ratio of  $I_{3/2}:I_{1/2} = 2$ . Green solid lines in (c) represent satellite peaks of Fe 2p orbitals. **d** Blue, red, and green curves correspond to O1, O2, and O3 peak fitting for O 1s spectrum, respectively.

information. Furthermore, the BEs value of the SOS pair at  $2p_{1/2}$   $BE_{Fe1} = 723.78$  eV and  $2p_{3/2}$   $BE_{Fe1} = 710.18$  eV is assigned to Fe1 atoms (peak3 and peak1, blue curves) for BaMF25mJ. In a similar way, the BE values of the SOS pair at  $2p_{1/2}$   $BE_{Fe2} = 726.4$  eV and  $2p_{3/2}$   $BE_{Fe2} = 712.8$  eV are assigned to Fe2 atoms (peak 4 and 2, red curves).

Figure 8d shows that the O 1s spectral region could be fitted to three sub-peaks. The lower binding energies  $BE_{O1} = 529.46$  eV and  $BE_{O2} = 531.53$  eV are labeled as O1 and O2, respectively, and are assigned to  $O^{2-}$  ions in the h-BaM phase. It is well known that the O 1s peak is in the binding energy range 528–531 eV and corresponds to metal oxide. On the other hand, the O3 atoms with  $BE_{O3} = 533.14$  eV is attributed to an oxidation state  $O^{x-}$  ( $0 < x < 2$ ) which

corresponds to chemisorbed species as well as to oxygen vacancies. The results of the peak profile fits, which include the peak positions and the integrated intensities of the Ba 3d, Fe 2p, and O 1s atoms, are summarized for the samples BaMF25mJ and BaMF75mJ in table (S2) of the supplementary information. It should be emphasized that the derived percentage is used to investigate the variation of the Fe/Ba ratio with the laser fluence, since the sum of the intensities  $I_{Ba} + I_{Fe} + I_O$  is 100% as exhibited in table (S2) of the supplementary information. In this study, we are concerned to explore the relative changes in the peak positions, shape, and intensity ratios between chemical elements arising from increasing the fluence from 25 to 75 mJ. In order to investigate the effect of the laser fluence on the

**Figure 9** Acquired XPS a survey spectrum with inset of magnified region of Fe 2 s, Fe 2p, and Ba 3d lines. b Ba 3d, c Fe 2p, and d O 1 s spectra of BaMF25mJ and BaMF75mJ films.



chemical composition of the surface, we compared the overall spectra of all elements, i.e., Ba, Fe, and O in Fig. 9a where the onset illustrates the spectra for Ba and Fe as a function of the laser fluence only. We should note that for BEs lower than 700 eV and higher than 820 eV, both spectra are well superposed, while in between, the intensities are different. In the BEs range, which corresponds to Fe, the red spectrum of the BaMF25mJ sample has a higher intensity than that of BaMF75mJ, while in the Bes, range of Ba the behavior is reversed and the blue profile of BaMF25mJ indicates that the intensities of Ba are higher for BaMF25mJ compared to BaMF75mJ. Figure 9b, c, and 9d specifically differentiate between the spectra of Ba, Fe, and O of the two BaMF25mJ and BaMF75mJ films. Additionally, by fitting all the spectra, the corresponding peak positions and intensities are determined and compared in table (S2) of the supplementary information. The comparison of the spectrum profiles shows that the Ba intensity is higher in the case of BaMF25mJ, while it is vice versa in the case of the Fe intensity. In fact, the integrated area is  $I_{Ba} = 14.35\%$  for BaMF25mJ and  $9.62\%$  for BaMF75mJ. Oppositely,  $I_{Fe} = 72.25\%$  for BaMF25mJ and  $77.75\%$  for BaMF75mJ. These results indicate that

BaMF25mJ is rich in barium and BaMF75mJ is Fe-rich. Furthermore,  $I_{O1} = 10.12\%$  is found to be higher in the case of BaMF25mJ.

#### *Stoichiometry and composition of BaM films in dependence on the laser fluence*

Combined STEM/EDXS analyses were performed to elucidate the element distribution and the chemical composition of the two different BaM films. In particular, X-ray maps were recorded in the STEM mode with an electron probe smaller than 1 nm in diameter. The obtained map data were subsequently quantified by using the thin-film approximation, i.e., the background contribution was subtracted, and an atomic number ( $Z$ ) correction was applied, however, absorption and fluorescence effects are not corrected. Moreover, line-profile analyses were carried out for selected regions of the TEM lamellas after the quantification of the maps. In order to improve the signal-to-noise ratio of these line-profile data, the corresponding values were averaged in the perpendicular direction relative to the direction of the chosen line which is marked with a red arrow in Fig. 10.



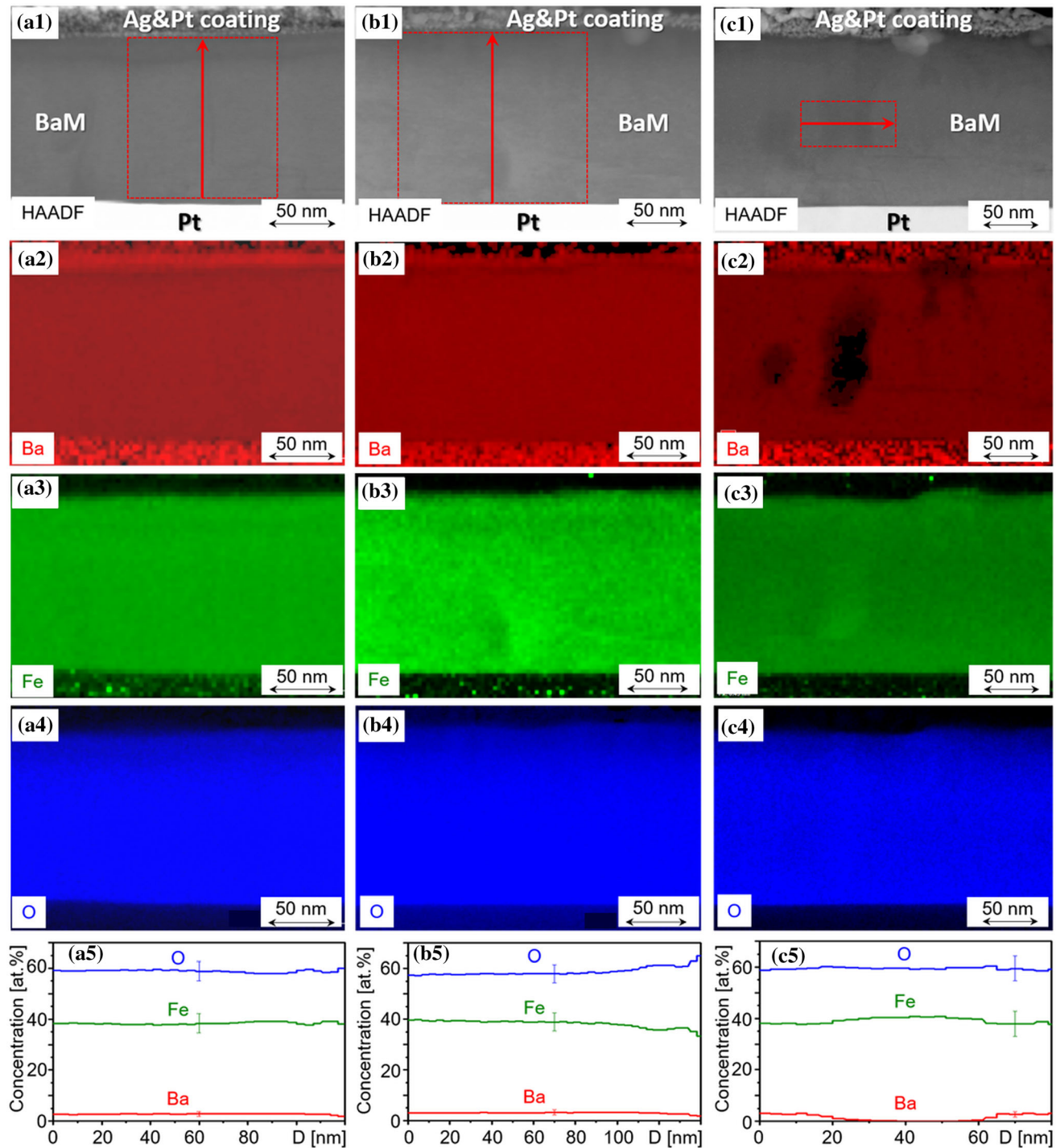


**Figure 10** Combined STEM/EDXS analysis of the element distribution of the BaM/Pt layers on YSZ in cross section: STEM HAADF images and X-ray maps of the distribution of the elements Ba, Fe, and O together with corresponding element-concentration profiles of the regions marked in the STEM HAADF images for BaMF25mJ **a1-a5** and for two different regions in BaMF75mJ, where figures **b1-b5** represent a typical BaM region

and **c1-c5** show a region with a secondary Fe–O-rich phase. The individual energy-dispersive X-ray data were quantified by using the thin-film approximation and the noise of the obtained maps was reduced by applying a  $3 \times 3$  mean filter. The error bars in the element-concentration profiles amount approximately 1 at. % for Ba, 4.5 at. % for Fe, 4.5 at. % for O.



For the BaMF25mJ and BaMF75mJ films, in this figure, typical X-ray maps of the elements Ba (red), Fe (green), and O (blue) are shown together with corresponding STEM HAADF images as well as element-concentration profiles. In general, the element maps allow to clearly differentiate between the BaM film and the underlying Pt interlayer, where the interface between them is flat and chemically sharp. The overall composition of the two films is close to the nominal value, namely approximately 3 Ba, 37 Fe, and 60 at% O. This is demonstrated in the corresponding quantitative EDXS line profiles depicted in Fig. 10a5 and b5. However, there are some little deviations from this chemical composition observable, which for both BaM films, particularly appear to be present in upper regions of the films. From Fig. 10a5, it can be deduced that in the case of BaMF25mJ, the composition of the BaM film is nearly constant across the whole layer thickness. Only in regions of about 20 nm below the surface, there are slight variations of the local concentrations of Ba, Fe, and O. The change of the local microchemistry in near-surface regions can hardly be interpreted as real inhomogeneity in the chemical composition due the probable artifact generated by the TEM sample preparation. In fact, the Ga<sup>+</sup> ion beam could cause this change during FIB milling.

In contrast, for BaMF75mJ (cf. Fig. 10b5), small gradients of the Fe and O contents can be seen that already start at the middle of the BaM film and extend toward its surface. In more detail, the Fe concentration seems to decrease steadily, whereas oxygen behaves vice versa. However, in the same range, the barium content appears to be constant, apart from the very near-surface region where barium is slightly depleted. For instance, in Fig. 10b5, at the bottom ( $D = 0$  nm) of the BaM film, the element composition is 3.0 at.% Ba, 39.5 at.% Fe, and 57.5 at.% O, whereas in the surface regions ( $D = 140$  nm), the values are Ba (1.8 at.%), Fe (33.3 at.%), and O (64.9 at.%). In addition, in the BaMF75mJ film, a secondary Fe–O phase was detected at some few positions for which the composition is approximately 40 at.% Fe and 60 at.% O hinting at iron oxide Fe<sub>2</sub>O<sub>3</sub>. (see Fig. 10c1–c5). However, compared to the BaM matrix material, its volume fraction is relatively low. In the respective TEM lamella, such Fe–O regions were only found at two positions with some distance of about 5 μm.

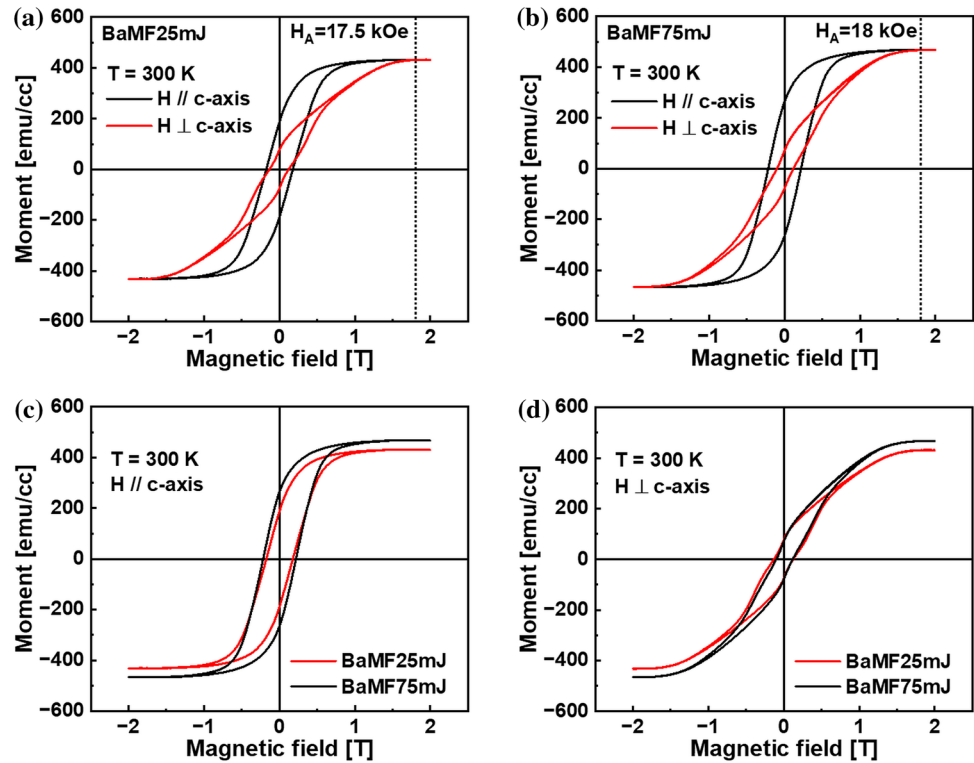
In summary, BaMF25mJ is found to be nearly homogenous with a stoichiometry similar to the target material, whereas BaMF75mJ displays a slight gradient in the chemical composition and, in addition, a secondary Fe–O phase, which leads to some depth-dependent deviation in the stoichiometry.

It should be emphasized that for both BaM films the chemical composition of near-surface regions is different from that of the volume, which is more pronounced for BaMF75mJ. This could partially explain the differences detected in the XPS spectra of the two BaM films. However, it should be noted that, because of the extremely small size ( $\leq 1$  nm) of the electron probe and a typical TEM lamella thickness of about 70 nm, the information of STEM/EDXS analyses is very local. This means that the spatial resolution of EDXS combined with STEM is much higher than that of XPS measurements, which averages over an area of about 1 mm in diameter. But the latter has a very high surface sensitivity in the order of approximately 15 nm. Moreover, STEM/EDXS analyses of surface regions in cross sections are complicated because of the BaM films roughness, which seems to be more distinct in the case of BaMF75mJ and the additional disturbance of surface areas by the deposition of Ag and Pt protection layers before TEM lamella preparation.

#### *Influence of the laser fluence on the magnetic properties*

Figure 11a and b show the out-of-plane and the in-plane hysteresis loops measured in the range [−2 T to 2 T] of the samples BaMF25mJ and BaMF75mJ films, respectively. For both samples, there is a significant difference between the in-plane and out-of-plane hysteresis loops. For BaMF75mJ, the high values of the out-of-plane squareness and the low value of in-plane squareness ( $S_{\perp} = 0.56$ ,  $S_{//} = 0.152$ ) indicate a high degree of crystallographic alignment in the film along  $c$ -axis direction. Furthermore, the comparison between the values of  $S_{\perp}$  and  $S_{//}$  of the two samples shows that the degree of orientation increases with the fluence. The anisotropy field  $H_A$  is found about 18 kOe (i.e., 1.8 T) for BaMF75mJ, while  $H_A$  is 17.5 kOe (i.e., 1.75 T) in the case of BaMF25mJ. The magnetization at the saturation  $M_s$  is found to be comparable as we grow similar film thicknesses of 140 nm for the BaMF25mJ and BaMF75mJ films by rescaling the number of shots. Figure 11c and d compares between the hysteresis loops of BaMF25mJ and BaMF75mJ. It

**Figure 11** In-plane and out-of-plane hysteresis loops of a BaMF25mJ, b BaMF75mJ, c Comparison between BaMF25mJ and BaMF75mJ of the out-of-plane magnetization loops, and d The in-plane hysteresis loops.



also shows that the hysteresis area and the coercive field  $H_c = 2166$  Oe are higher in the case of BaMF75mJ. This indicates that the dissipation energy is large because of the high defect density as it has already been demonstrated by HRTEM for BaMF75mJ. Furthermore, the presence of the minor of the  $\text{Fe}_2\text{O}_3$  secondary phase and the interaction between BaM and Fe–O phase could also contribute additionally to the enhancement of coercive field  $H_c$ .

Nevertheless, the resulting increase of the coercive field  $H_c$  with the fluence will have most probably an advantageous impact in the improvement of the recording resolution of the perpendicular medium.

## Conclusions and discussions

The effect of increasing the energy per pulse from 25 to 75 mJ on the microstructure, morphology, chemical composition, and magnetic properties of PLD-grown BaM hexaferrite films was studied in detail by using a combination of complementary methods such as HR-XRD, AFM, XPS, HRTEM, STEM/EDXS, and VSM. Since the laser fluence affects the kinetic energy of the species ablated from the BaM target, the resulting difference in the diffusion energy of the

impinging species on the substrate surface led to the growth of different films having different morphologies. In fact, two types of outgrowth were detected in AFM micrographs of BaMF75mJ. We demonstrate by means of HRTEM and HR-XRD that both films BaMF25mJ and BaMF75mJ display a good epitaxial growth on the Pt(111) interlayer and are composed of mosaic blocks which are separated by defects located at the boundaries. In comparison with BaMF25mJ where only mosaic blocks boundaries exist in the lateral direction, BaMF75mJ additionally contains mosaic boundaries in the vertical direction indicating a high density of defects. This, in turn, has enhanced the misorientation degree of the mosaic blocks as it could be confirmed by HRTEM imaging and the large angular broadening of XRD diffraction profiles. Regarding the stoichiometry of the grown films, EDXS mapping demonstrates a stoichiometry transfer between the BaM target and the grown film BaMF25mJ. However, BaMF25mJ appears to be more homogenous in the stoichiometry than BaMF75mJ, which shows depth-dependent element-concentration profiles and a secondary Fe–O phase. In conclusion, the increase of the laser fluence induced more crystal defects in the grown film, in particular, more mosaic-block boundaries in the form of out-of-

**Table 3** Energy per pulse, growth rate (GR), saturation magnetization ( $M_s$  +), remanence magnetization ( $M_r$  +), out-of-plane magnetic squareness ( $S_{\perp}$ ), in-plane magnetic squareness ( $S_{\parallel}$ ), magnetic coercivity ( $H_c$  +), perpendicular anisotropy ( $H_{c_{\perp}}/H_{c_{\parallel}}$ ) and grain sizes of BaMF25mJ and BaMF75mJ films

	Energy per pulse (fluence)	GR (nm/min)	$M_s$ + [emu/cc]	$M_r$ + [emu/cc]	$S_{\perp} = M_r_{\perp}/M_s_{\perp}$	$S_{\parallel} = M_r_{\parallel}/M_s_{\parallel}$	$H_c$ + [Oe]	$H_{c_{\perp}}/H_{c_{\parallel}}$	Interconnected hexagonal chains [nm] [min–max]	Grain sizes [nm] [min–max]
BaMF25mJ	Out-of-plane	0.41	430	185	0.43		1768.9	0.70	[287–983]	[450–800]
	In-plane	0.41	430	76		0.177	1253.4			
BaMF75mJ	Out-of-plane	1.22	467	262	0.56		2166.0	0.53	[301–740]	[80–265]
	In-plane	1.22	462	70		0.152	1177.3			

phase boundaries and a secondary Fe–O phase, which disturbs the film stoichiometry at a few locations. This has an impact on the magnetization hysteresis loop and the coercive field. However, BaMF75mJ film was demonstrated to be more suitable for recording media application due to the small grain size, higher squareness, and larger coercivity in comparison with BaMF25mJ (Table 3).

This detailed and deep study has enabled us to demonstrate the importance of the laser fluence as a PLD growth parameter, which can be utilized to modulate the microstructure, morphology, and the resulting magnetic properties of BaM films with respect to its specific material applications.

### Acknowledgements

The work was supported by the Czech Science Foundation (project No. 19-10799J) and by the project NanoCent financed by European Regional Development Fund (ERDF, project No. CZ.02.1.01/0.0/0.0/15.003/0000485). The additional funding of this study by the German Research Foundation within the framework of the projects SCHN 669/11 and BA 1642/8-1 is also gratefully acknowledged. We acknowledge to KIT light source for providing the equipments at their beamlines. We also would like to thank to Institute for Beam Physics and Technology (IBPT) for operation of the storage ring, providing the beam in Karlsruhe Research Acceleration (KARA). XPS measurements were conducted in UHV laboratory in KARA. We would like to thank Dr. Bärbel Krause for allowing to use UHV laboratory equipments. In this work, Atomic Force Microscopy (AFM) measurements were carried out with the support of the Karlsruhe Nano Micro Facility (KNMF-i, [www.knmf.kit.edu](http://www.knmf.kit.edu)), a Helmholtz Research Infrastructure at Karlsruhe Institute of Technology (KIT, [www.kit.edu](http://www.kit.edu)). We would like to thank Mr. Richard Thelen and apl. Prof. Dr. Hendrik Hölscher for allowing us to use their AFM facility.

### Funding

Open Access funding enabled and organized by Projekt DEAL.

## Declarations

**Conflicts of interest** The authors declare that they have no known competing financial interests or personal relationships that could have appeared to influence the work reported in this paper.

**Supplementary Information:** The online version contains supplementary material available at <http://doi.org/10.1007/s10853-022-08104-9>.

**Open Access** This article is licensed under a Creative Commons Attribution 4.0 International License, which permits use, sharing, adaptation, distribution and reproduction in any medium or format, as long as you give appropriate credit to the original author(s) and the source, provide a link to the Creative Commons licence, and indicate if changes were made. The images or other third party material in this article are included in the article's Creative Commons licence, unless indicated otherwise in a credit line to the material. If material is not included in the article's Creative Commons licence and your intended use is not permitted by statutory regulation or exceeds the permitted use, you will need to obtain permission directly from the copyright holder. To view a copy of this licence, visit <http://creativecommons.org/licenses/by/4.0/>.

## References

- [1] Futamoto M, Hirayama Y, Honda Y, Kikukawa A (2001) Perpendicular recording media for ultra-high-density magnetic recording. In: Hadjipanayis GC (ed) Magnetic storage systems beyond 2000 NATO science series. Springer
- [2] Kryder MH, Gustafson RW (2005) High-density perpendicular recording—advances, issues, and extensibility. *J Magn Magn Mater* 287:449–458
- [3] Nakagawa Sh, Matsushita N, Naoe M (2001) Perpendicular magnetic recording media using hexagonal ferrite thin films deposited on Pt underlayers and interlayers. *J Magn Magn Mater* 235:337–341
- [4] Cherubini G, Cideciyan RD, Dellmann L et al (2011) 29.5-Gb/in<sup>2</sup> recording areal density on barium ferrite tape. *IEEE Trans Magnetics* 47(1):137–147. <https://doi.org/10.1109/TMAG.2010.2076797>
- [5] Alahmed L, Li P. (2020) Perpendicular magnetic insulator films for Spintronics, <https://doi.org/10.5772/intechopen.92277>. doi: <https://doi.org/10.5772/intechopen.92277>
- [6] Yoon SD, Vittoria C, Oliver SA (2003) Magnetic and microwave magnetic properties of barium hexaferrite permanent magnet films having the *c*-axis in the film plane. *J Appl Phys* 93:4023–4026. <https://doi.org/10.1063/1.1544083>
- [7] Harris VG, Chen Zh, Chen Y, Yoon S, Sakai T, Gieler A, Yang A, He Y (2006) Ba-hexaferrite films for next generation microwave devices. *J Appl Phys* 99:08M911. <https://doi.org/10.1063/1.2165145>
- [8] Zhang X, Meng S, Song D, Zhang Y, Yue Zh, Harris VG (2017) Epitaxially grown BaM hexaferrite films having uniaxial axis in the film plane for self-biased devices. *Sci Rep* 7:44193. <https://doi.org/10.1038/srep44193>
- [9] Zhaohui Ch, Fan Y (2016) Barium hexa-ferrite technology for MAMR and advanced magnetic recording applications. <https://patents.google.com/patent/GB2552022A/en>.
- [10] Li X, Tan GL (2021) Multiferroic and magnetoelectronic polarizations in BaFe<sub>12</sub>O<sub>19</sub> system. *J. Alloys Compd* 858:157722. <https://doi.org/10.1016/j.jallcom.2020.157722>
- [11] Kumar P, Gaur A (2019) *Appl. Phys. A* 125:6296. <https://doi.org/10.1007/s00339-019-2928-7>
- [12] Vinnik DA, Zhivulin VE, Starikov AYU et al (2020) Influence of titanium substitution on structure, magnetic and electric properties of barium hexaferrites BaFe<sub>12-x</sub>Ti<sub>x</sub>O<sub>19</sub>. *J Magn Magn Mater* 498:166117
- [13] Liu H, Avrutin V, Xiao Bo E, Rowe HR, Liu ÜÖ, Morkoç H (2010) Epitaxial relationship of MBE grown barium hexaferrite (0001) films on sapphire (0001). *J Cryst Growth* 312:671–675. <https://doi.org/10.1016/j.jcrysgro.2009.12.013>
- [14] Ohodnicki PR, Goh KY, McHenry ME, Ziemer K, Chen Z, Vittoria C, Harris VG (2008) Correlation between texture, anisotropy, and vector magnetization processes investigated by two-dimensional vector vibrating sample magnetometry in BaO(Fe<sub>2</sub>O<sub>3</sub>)<sub>6</sub> thin film. *J Appl Phys* 103:07E514. <http://doi.org/10.1063/1.2838630>
- [15] Yoon SD, Vittoria C (2004) Thick M-type barium hexaferrite films grown on garnet substrates. *J Appl Phys* 96:2131–2135. <https://doi.org/10.1063/1.1769597>
- [16] Geiler AL, Yang A, Zuo Xu, Yoon SD, Chen Y, Harris VG, Vittoria C (2008) Atomic scale design and control of cation distribution in hexagonal ferrites. *Phys Rev Lett* 101:067201. <https://doi.org/10.1103/PhysRevLett.101.067201>
- [17] Mohebbi M, Ebnabbasi K, Vittoria C (2013) In-situ deposition of *c*-axis oriented barium ferrite films for microwave applications. *IEEE Trans Magn* 49:4207–4209. <https://doi.org/10.1109/Tmag.2013.2250491>
- [18] Zhang L, Su XD, Chen Y, Li QF, Harris VG (2010) Radio-frequency magnetron sputter-deposited barium hexaferrite films on Pt-coated Si substrates suitable for microwave



- applications. *Scripta Mater* 63:492–495. <https://doi.org/10.1016/j.scriptamat.2010.05.013>
- [19] Abuzir AR, Salman SA (2018) Fabrication and micromagnetic modeling of barium hexaferrite thin films by RF magnetron sputtering. *Results Phys* 8:587–591. <https://doi.org/10.1016/j.rinp.2018.01.003>
- [20] Zhou E, Zheng H, Zheng P, Zheng L, Deng J, Qin H (2016) The influence of oxygen pressure on the crystallographic structure and magnetic properties of BaM films on Al<sub>2</sub>O<sub>3</sub>(0001) substrate. *Adv Eng Res* 93:67–72
- [21] Oliver SA, Chen ML, Kozulin I, Vittoria C (2000) Structure and magnetic properties of barium hexaferrite films deposited at low oxygen pressures. *J Magn Magn Mater* 213(3):326–334. [https://doi.org/10.1016/S0304-8853\(00\)00004-4](https://doi.org/10.1016/S0304-8853(00)00004-4)
- [22] Wie X, Zheng H, Chen W, Wu Q, Zheng P, Zheng L, Zhang Y (2020) Crystal structure, morphology and magnetic properties of hexagonal M-type barium ferrite film based on the substrate temperature. *Chem Phys Lett* 752:137541–1–137541-4. <https://doi.org/10.1016/j.cplett.2020.137541>
- [23] Zandalazini CI, Oliva MI, Ferrero JC (2012) Influence of the oxygen pressure and annealing time in the magnetic and structural properties of barium ferrite thin films. *Revista Mexicana de Física* 58(2):266–269
- [24] Chen DM, Li YX, Han LK, Long Ch, Zhang HW (2016) Perpendicularly oriented barium ferrite thin films with low microwave loss, prepared by pulsed laser deposition. *Chin Phys B* 25(6):068403. <https://doi.org/10.1088/1674-1056/25/6/068403>
- [25] Dorsey PC, Chrisey DB, Horwitz JS, Lubitz P, Auyeung RCY (1994) Oriented barium hexaferrite thick films grown on c-plane and m-plane sapphire substrates. *IEEE Trans Magn* 30(6):4512–4517. <https://doi.org/10.1109/20.334133>
- [26] Shinde SR, Lofland SE, Canpule CS, Ogale SB, Bhagat SM, Ramesh VT, R, (1999) Realization of epitaxial barium ferrite films of high crystalline quality with small resonance losses. *J Appl Phys* 85(10):7459–7466. <https://doi.org/10.1063/1.369379>
- [27] Zhuang Z, Rao M, Laughlin DE, Kryder MH (1999) The effect of Pt interlayers on the magnetic and structural properties of perpendicularly oriented barium ferrite media. *J Appl Phys* 85(8):6142–6144. <https://doi.org/10.1063/1.370023>
- [28] Liu XH, Hong MH, Song WD, Chen GX, Chong JF, Wang JP, Wu YH, Chong TC (2004) Pulsed laser deposition of oriented barium ferrite (BaFe<sub>12</sub>O<sub>19</sub>) thin films. *Appl Phys A* 78(3):423–425. <https://doi.org/10.1007/s00339-002-1957-8>
- [29] Zheng H, Zheng L, Zheng P, Deng JX, Ying ZH, Qin HB (2017) Effect of Pt buffer layer on crystal structure and magnetic properties of hexagonal barium ferrite films. *Mat Lett* 190:263–265. <https://doi.org/10.1016/j.matlet.2017.01.029>
- [30] Zheng H, Luo J, Wu Q, Zhenga P, Zhenga L, Hanc M, Zhanga Y (2019) Hexagonal barium ferrite films on a Pt(1 1 1)/Si(0 0 1) substrate and their local magnetic properties. *J Magn Magn Mater* 479:99–104. <https://doi.org/10.1016/j.jmmm.2019.02.024>
- [31] Suzuki D, Sakamoto N, Shinozaki K, Suzuki H, Wakiya N (2013) Magnetic field effects during deposition on crystal structure and magnetic properties of BaFe<sub>12</sub>O<sub>19</sub> thin films prepared using PLD in the magnetic field (Dynamic aurora PLD). *J C S Japan* 121(1409):45–48. <https://doi.org/10.2109/jcersj2.121.45>
- [32] Papakonstantinou P, O'Neill M, Atkinson R, Salter IW, Gerber R (1996) Oriented barium, strontium ferrite films pulsed laser deposited on YSZ (100) and Si (100) substrates. *J Magn Soc Jpn* 20(S1):333–336
- [33] Zhuang Z, Rao M, White RM, Laughlin DE, Kryder MH (2000) Barium ferrite thin film media with perpendicular c-axis orientation and small grain size. *J Appl Phys* 87:6370–6372. <https://doi.org/10.1063/1.372709>
- [34] Yu Ch, Sokolov AS, Kulik P, Harris VG (2020) Stoichiometry, phase, and texture evolution in PLD-grown hexagonal barium ferrite films as a function of laser process parameters. *J Alloys Compd* 814:152301–1–152301-8. <https://doi.org/10.1016/j.jallcom.2019.152301>
- [35] Ojeda-G-P A, Döbeli M, Lippert Th (2018) Review: Influence of plume properties on thin film composition in pulsed laser deposition. *Adv Mater Interfaces* 5:1701062–2–1701062-16. <https://doi.org/10.1002/admi.201701062>
- [36] Jaber N, Wolfman J, Daumont C, Négulescu B, Ruyter A, Sauvage T, Courtois C, Bouyanfif H, Longuet JL, Autret-Lambert C, Gervais F (2017) Laser fluence and spot size effect on compositional and structural properties of BiFeO<sub>3</sub> thin films grown by pulsed laser deposition. *Thin Solid Films* 634:107–111. <https://doi.org/10.1016/j.tsf.2017.05.003>
- [37] Ohnishi T, Koinuma H, Lippmaa M (2006) Pulsed laser deposition of oxide thin film. *Appl Surf Sci* 252:2466–2471. <https://doi.org/10.1016/j.apsusc.2005.04.057>
- [38] Fähler S, Krebs HU (1996) Calculations and experiments of material removal and kinetic energy during pulsed laser ablation of metals. *Appl Surf Sci* 96–98:61–65. [https://doi.org/10.1016/0169-4332\(95\)00466-1](https://doi.org/10.1016/0169-4332(95)00466-1)
- [39] Schou J (2009) Physical aspects of the pulsed laser deposition technique: The stoichiometric transfer of material from target to film. *Appl Surf Sci* 255(10):5191–5198. <https://doi.org/10.1016/j.apsusc.2008.10.101>
- [40] Zhang XY, Ong CK, Xu SY, Fang HC (1999) Observation of growth morphology in pulsed-laser deposited barium ferrite

- thin films. *Appl Surf Sci* 143(1–4):323–327. [https://doi.org/10.1016/S0169-4332\(99\)00100-2](https://doi.org/10.1016/S0169-4332(99)00100-2)
- [41] Gabriel V, Kocán P, Bauer S et al (2022) Effect of pulse laser frequency on PLD growth of LuFeO<sub>3</sub> explained by kinetic simulations of in-situ diffracted intensities. *Sci Rep* 12:5647. <https://doi.org/10.1038/s41598-022-09414-3>
- [42] Bauer S, Lazarev S, Molinari A, Breitenstein A, Leufke P, Kruk R, Hahn H, Baumbach T (2014) The power of in situ pulsed laser deposition synchrotron characterization for the detection of domain formation during growth of Ba<sub>0.5</sub>Sr<sub>0.5</sub>TiO<sub>3</sub> on MgO. *J Synchr Rad* 21:386–394. <https://doi.org/10.1107/S1600577513034358>
- [43] Williamson GK, Hall WH (1953) X-ray line broadening from filed aluminium and wolfram. *Acta Metall* 1:22–31
- [44] G. Cliff GW, Lorimer GW, (1975) The quantitative analysis of thin specimens. *J Microsc* 103:203–207
- [45] Fityk MW (2010) a general-purpose peak fitting program. *J Appl Cryst* 43:1126–1128
- [46] CasaXPS Processing Software, CasaXPS Manual 2.3.15 Rev 1.2 Casa Software Ltd, Copyright © 2009
- [47] Anthony MT, Seah MP (1984) XPS: Energy calibration of electron spectrometers 2-Results of an interlaboratory comparison. *Surf Interface Anal* 6:107–115
- [48] Moulder JF, Stickle WF, Sobol PE, Bomben KD. J. Ed: Perkin Elmer Corporation: Eden Prairie, MN, 1992
- [49] Atuchin VV, Vinnik DA, Gavrilova TA, Gudkova SA, Isaenko LI, Xingxing J, Pokrovsky LD, Prosvirin IP, Mashkovtseva LS, Lin Zh (2016) Flux crystal growth and the electronic structure of BaFe<sub>12</sub>O<sub>19</sub> hexaferrite. *J Phys Chem C* 120:5114–5123. <https://doi.org/10.1021/acs.jpcc.5b12243>

**Publisher's Note** Springer Nature remains neutral with regard to jurisdictional claims in published maps and institutional affiliations.